The Astrophysical Journal, 978:80 (11pp), 2025 January 01 https://doi.org/10.3847/1538-4357/ad9399

Pulse-profile Modeling and Spin–Orbit Alignment in a Suzaku Sample of Accreting X-Ray Binary Pulsars

Silas G. T. Laycock[1,2], Rigel C. Cappallo[3], Pragati Pradhan[4,5], Dimitris M. Christodoulou[1,2], and Biswajit Paul[6]
[1] University of Massachusetts Lowell, Kennedy College of Sciences, Lowell, MA, 01854, USA
[2] Lowell Center for Space Science and Technology, Lowell, MA, 01854, USA
[3] Massachusetts Institute of Technology, Haystack Observatory, Westford, MA, 01886, USA
[4] Massachusetts Institute of Technology, Kavli Institute for Astrophysics and Space Research, Cambridge, MA, 02139, USA
[5] Embry-Riddle Aeronautical University, 3700 Willow Creek Road, Prescott, AZ, 86301, USA
[6] Raman Research Institute, Astronomy and Astrophysics, Bangalore, 560080, India
Received 2024 February 6; revised 2024 October 2; accepted 2024 October 2; published 2024 December 26

Abstract

We report pulse-profile modeling of a sample of 23 X-ray binary pulsars observed with the Suzaku X-ray satellite. These pulsars have spin periods ranging from 0.7 to 9400 s, and their X-ray emission is powered by the accretion from their stellar companions. We fitted each individual pulse profile with the Polestar geometric model, which accounts for X-ray emission from two hot spots modeled as a simple combination of fan+pencil beam components, including an approximation for gravitational light bending. In 14 of 21 cases, our measurements of the inclinations of the pulsar spin axes broadly agree with the corresponding inclinations of the orbital planes of the binary systems determined by various other means, a striking outcome with a mere 6×10^{-7} probability of occurring by chance. The implications of our study are as follows: (a) apparently, accretion torques have had time to erase spin–orbit misalignment caused by supernova kicks in two-thirds of the systems; (b) many X-ray binary pulsars have dominant dipolar surface magnetic fields, in contrast to the recently reported exotic configurations in millisecond pulsars; and (c) if the binary inclinations can be determined by pulse-profile modeling, even for a subset of the ∼200 known X-ray binary pulsars, most of which orbital inclinations are as yet poorly constrained, it raises the prospect of tightening dramatically ongoing neutron-star mass determinations. This is because masses in binary systems overwhelmingly come from an orbital-mechanics formulation (Kepler's third law), in which the dominant source of uncertainty is the inclination of the orbital plane.

Unified Astronomy Thesaurus concepts: Pulsars (1306)

Materials only available in the online version of record: data behind figures

1. Introduction

Modeling of X-ray pulsar pulse profiles offers a means to indirectly obtain intrinsic properties of neutron stars (NSs), such as spin-axis inclination, magnetic obliquity, and compactness, and by extension, to constrain the equation of state (A. L. Watts et al. 2016). At the same time, because the X-ray beam pattern is shaped by the structure of the pulsar magnetosphere, information about the three-dimensional accretion flow is also encoded in the pulse profile (A. N. Parmar et al. 1989; U. Kraus et al. 1996). These phenomena are intertwined, and consequently, pulse-profile modeling (PPM) suffers an inherent nonuniqueness problem unless some additional independent constraints can be obtained and used to break the degeneracies among model parameters.

This investigation is partly motivated by such concerns. In particular, orbital inclinations have been determined for many high-mass X-ray binary pulsars (HMXBPs), and these inclinations can be compared against pulsar spin-axis inclination values inferred by PPM. In this way, we can assess the validity of PPM-derived parameters. For this study, we fit a set of 23 Suzaku pulse profiles, using the PPM code Polestar (R. Cappallo et al. 2017), which implements a two-magnetic-pole, two-component (per pole) beam emission pattern including an approximation of gravitational light bending. Polestar was developed to model large samples of HMXBP pulse profiles in order to then perform statistical studies of the fitted parameter values.

1.1. Pulsar Classes

The X-ray pulsars in this study are accreting, that is, they are fed by matter being shed by the companion star; accreted matter forms mounds, shocks, and columns above the NS surface (P. A. Becker & M. T. Wolff 2005). In this sense, HMXBPs differ from millisecond pulsars (MSPs), which have been typically/conventionally modeled with relatively simpler (but still complex) emission geometries (e.g., J. Poutanen et al. 2009). In principle, MSPs offer the best path to intrinsic NS properties, and they have been the test bed of recent significant progress in PPM. The Neutron Star Interior Composition Explorer (NICER) mission has enabled a flood of new PPM-deduced results for MSPs (M. C. Miller et al. 2019; T. E. Riley et al. 2019), which suggest that NSs are even more complex than previously thought, challenging long-held assumptions about the nature of pulsars. Seemingly answered questions such as "How many emitting hot spots are there?" and "Does the pulsar magnetic field have a predominantly dipolar structure?" have recently been cast to open debate (M. C. Miller et al. 2019; C. Kalapotharakos et al. 2021). At the same time, long-sought physical parameters are being measured, such as mass, radius, spin inclination, and magnetic axis offsets from the spin

axis recently determined for MSPs (T. E. Riley et al. 2019; J. Pétri et al. 2023) and HMXBPs (R. Cappallo et al. 2019; R. C. Cappallo et al. 2020; V. Doroshenko et al. 2022; Y. F. Hu et al. 2023).

X-ray binary pulsars (XBPs) also differ from radio pulsars (V. S. Beskin et al. 2015; V. S. Beskin 2018) and γ-ray pulsars (C. Kalapotharakos et al. 2022) in significant ways, including the sites and the mechanisms of radiation emission, the pulse period distributions, and their formation/evolution channels. Radio and γ-ray pulsars are also overwhelmingly isolated systems. In marked contrast, X-ray pulsars are not only commonly found in binary systems, but they are often assumed to exhibit spin–orbit alignment as well, in which the rotation axis is considered to be parallel to the orbital angular momentum vector (e.g., U. Kraus et al. 1995, 1996, 2003; A. Biryukov & P. Abolmasov 2021). We have an opportunity to test this customary hypothesis in the present work.

1.2. Supergiant and Be X-Ray Binaries

In a binary system containing at least one star of 8–10 or more solar masses ($M_\odot$), the initially more massive star will reach the supernova (SN) stage first during evolution. Provided that the binary survives the SN explosion, and depending on the mass and evolutionary state of the stellar companion, the newly formed compact object, an NS or a black hole, will accrete matter from the companion, and it will thus emerge as an X-ray source. HMXBs are those binaries in which a massive $\sim 10\,M_\odot$ star (the "primary") is the mass donor. In the majority (>80%) of identified systems in the Milky Way and the Magellanic Clouds, the primary is a Be star (V. A. McBride et al. 2008) possessing a circumstellar disk (CD) that acts as a reservoir of fuel for the orbiting compact object. In the remaining systems, the primary is an O or B supergiant, whose extended wind provides the fuel for accretion-powered X-ray emission. Both types are represented by 21 systems in the sample of 23 XRBs analyzed in this work.

Supergiant (SG) and Be X-ray binaries (Be-XRBs) differ in their X-ray properties in some important ways: SG-XRBs emit X-rays continually at X-ray luminosities $L_X \sim 10^{35}$–10^{36} erg s^{-1}, while Be-XRBs are transient emitters reaching $L_X > 10^{37}$ erg s^{-1} for days at a time although they spend most of their time in deep quiescence (for reviews, see P. Reig 2011 and D. M. Christodoulou et al. 2016). Thus, Be-XRBs constitute a subclass in which we study the effects of varying accretion rates, whereas SG-XRBs exhibit generally consistent, stable pulse profiles.

The X-ray flux emitted from the compact object in an XRB can be modulated by eclipses if the orbital plane lies close to our line of sight. Such a geometry conveniently places a strong constraint on the orbital inclination angle (e.g., J. B. Coley et al. 2015). Eclipses are most common among SG-XRBs as a consequence of their small orbital separations, on the order of several stellar radii. At these separations, tidal interactions rapidly circularize the orbits leading to little variation in the wind density and velocity encountered by the compact object, which thus becomes a persistent X-ray source. In contrast, very different conditions govern the X-ray emission from transient Be-XRBs, owing to the complex interaction between the wide (by many astronomical units) elliptical NS orbit and the CD surrounding the Be primary (Figure 1). Episodic accretion occurs during periastron passage of the NS, during which the

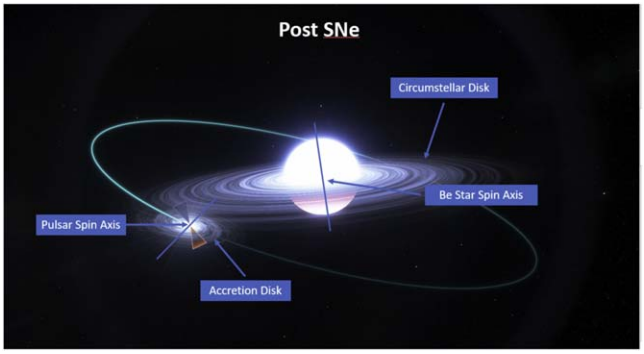

Figure 1. A Be XBP system. The NS, surrounded by a small accretion disk, feeds on matter being shed from its massive companion via its large equatorial CD. The spin axes of the two stars are shown by blue vector arrows. The orbital angular momentum vector lies perpendicular to the orbital plane. We chose to illustrate a disrupted system with misaligned spins, as would be the case following the SN explosion that produced the NS. Our study shows that, on the contrary, most X-ray pulsars have been "righted" by accretion and tidal torques, such that the orientations of pulsar spin and orbital angular momentum vectors coincide.

CD is tidally disturbed (A. T. Okazaki & I. Negueruela 2001), leading to a high mass-transfer rate onto the NS.

Many XRB systems exhibit a spin–orbit equilibrium arising from the interaction between the magnetic field of the NS and the angular momentum of the infalling plasma. This equilibrium results in SG and Be systems populating distinct regions in the $P_{\rm spin}$–$P_{\rm orbit}$ plane (the well-known Corbet diagram; R. H. D. Corbet 1984). At birth, NSs are imbued with spin periods in the millisecond range; thus, in order to emerge as HMXBPs, they must first slow down under the cumulative effects of accretion torques and magnetic stresses and via a propeller phase lasting potentially for millions of years but still being shorter than the main-sequence lifetimes of the $\geqslant 10\,M_\odot$ donor stars (N. R. Ikhsanov 2007). Such spin-up/-down trends in the HMXB population of the Small Magellanic Cloud (SMC) and their implications for fundamental physics are described by H. Klus et al. (2014) and D. M. Christodoulou et al. (2017).

1.3. Pulse-profile Modeling

This investigation is concerned with XRBs harboring strongly magnetized NSs. As the NS rotates about its spin axis, different parts of the accretion regions (related to the footprints of the inner closed magnetic field lines on the poles) come into view, leading to the popular "lighthouse" model of a pulsar.

(a) *Accretion structures*. In X-ray pulsars, the situation becomes complex, as the impact sites of the accreted material will be dense, extended, and quite hot. Each of these sites is thought to contain 3D structures commonly referred to as the "accretion mound" (a mountain of accreted material reaching perhaps 10–100 m in height) and the "accretion column" (an extended vertical region of infalling matter; P. A. Becker & M. T. Wolff 2007; B. F. West et al. 2017).

(b) *Shocks*. Depending on the strength of the magnetic field and the accretion rate, a standing shock may form above the NS surface, acting as a particle accelerator. The pulsar emission will thus include contributions from thermal, bremsstrahlung, and synchrotron radiation processes (B. F. West et al. 2017). In addition, the accretion column probably exerts a self-shadowing effect, whereby the dense matter absorbs some of the

outgoing radiation but only in certain directions (predominantly along the column's own axis).

(c) *Radiation emission*. The geometry of the polar caps, mounds, and accretion columns together creates a pair of beams (one from each magnetic pole) whose complex 3D shape is thought to vary between isotropic, a more collimated form (the "pencil beam"), and a hollowed-out cone-like form (the "fan beam"; M. M. Basko & R. A. Sunyaev 1976; A. N. Parmar et al. 1989). These components may be present simultaneously or in isolation, and their relative strengths could be different for each of the two magnetic poles. As the radiation finally leaves the NS surface, it climbs out of the gravitational potential well, experiencing the strong-field regime of general relativity (GR). Thus, the X-ray pulse profiles that are observed are heavily modified by the light-bending properties of GR (A. M. Beloborodov 2002).

(d) *Pulse profiles*. Existing pulse profile modeling efforts have ranged from the geometric model introduced by Y. M. Wang & G. L. Welter (1981) to fan and pencil beams, along with approximate GR corrections (A. N. Parmar et al. 1989), to Fourier-decomposition-based models (U. Kraus et al. 1995, 1996; S. Blum & U. Kraus 2000). Recent application of the Fourier-decomposition technique to a large sample of XMM-Newton and NuSTAR pulse profiles by J. Alonso-Hernández et al. (2022) has shown promise in identifying distinct pulse profile morphological classes. Somewhat surprisingly, these classes did not correlate strongly with other observables. Given the complexity of the problem (e.g., the exact geometrical structure of the accretion column is still not known), every model relies on some reasonable assumptions, e.g., a cylindrical accretion column, a dipolar magnetic field (A. N. Parmar et al. 1989), and/or that the emission sites are antipodal and that the sources of radiation are isotropic (A. M. Beloborodov 2002).

(e) *Modeling complexities*. The exceptional work of S. Falkner (2018) has recently shown that construction of detailed, fully 3D models incorporating the full gamut of radiative processes is possible and that such models can accurately reproduce the observed pulse profiles, including many of the energy-dependent fine details. The downside of incorporating such complexities in the models is that they seem to limit our ability to uniquely constrain the emerging accretion structures and radiation processes, as well as their physical properties. The advent of X-ray polarization data from IXPE (V. Doroshenko et al. 2022) as well as improved computational techniques, is changing this outlook.

1.4. Polestar Models

Polestar (R. Cappallo et al. 2017) implements a generalized class of fan and pencil models with light bending. It is intended to enable large numbers of pulse profiles to be processed and parameterized in the context of the most commonly discussed physical and geometrical pulsar variables. Given the inherent lack of detailed physics in these models, it is probable that not all pulse profiles will be adequately described in this way. Nevertheless, testing such models against a wide range of observed profiles is a useful first step that may reveal underlying physical relationships or establish clusters of interdependent NS parameter values in the overall parameter space, as was described by J. Alonso-Hernández et al. (2022). We note that similar pulse-profile models have also been developed for radio and γ-ray pulsars, in which inclination and magnetic obliquity angles have been measured for growing samples recently (M. Pierbattista et al. 2016; J. Pétri & D. Mitra 2021).

1.5. Experimental Design and Outline

In addition to performing PPM in a Suzaku data set of 23 bright XRB pulsars (most of which are Galactic HMXBPs), we also designed a double-blind experiment to test the hypothesis that NS spin axes would be aligned with their orbital angular momentum vectors. One of us (P.P.) collated a sample of 23 high signal-to-noise (S/N) pulse profiles from the Suzaku Hard X-ray Detector (HXD) instrument, one profile for each of the 23 XRBs (Table 1). Data collection and the construction of pulse profiles are described in Section 2.

The files were stripped of identifying metadata and transmitted to another member of the team (R.C.) working at a different location. R.C. ran the PPM code Polestar on each of the profiles and tabulated the resulting inclination angles of the NS spin axes, as well as additional model parameters. The results from modeling are described in Section 3. P.P. and B.P. were then asked to reveal the pulsar identifiers and to provide the published orbital inclination angles, as these were determined by other means (e.g., from optical spectroscopy or pulse timing studies).

In the comparative study that followed, we found that 21 of the 23 pulsars had published orbital inclination angles and corresponding uncertainty ranges and that 14 of the 21 pulsars had inclinations determined by Polestar that were in broad agreement with those known for the binaries from the literature. Finally, the reported and derived inclination ranges were compared by means of Monte Carlo simulations and the related analytical Poisson-binomial probability distribution, as described in Section 4. Our results are discussed in a broader context in Section 5, and we summarize our conclusions in Section 6.

2. X-Ray Observations and Data Collection

Suzaku (H. Kunieda et al. 2006) is a broadband X-ray (0.2–600 keV) observatory with two main instruments: the X-ray Imaging Spectrometer (XIS; K. Koyama et al. 2007) and the Hard X-ray Detector (HXD). The XIS consists of four CCD detectors of which three (XIS 0, 2, and 3) are front illuminated and one (XIS 1) is back illuminated. Each XIS covers the soft X-ray band of 0.2–12 keV. The HXD comprises PIN diodes (M. Kokubun et al. 2007) that cover the 10–70 keV energy range and GSO crystal scintillator detectors that cover the 70–600 keV energy range. Since the soft X-rays from the pulsar may undergo absorption along the line of sight, for the purposes of this work, we have used HXD/PIN pulse profiles that are more representative of the X-ray beaming patterns.

In order to extract the pulse profiles, we have used the filtered and cleaned event files obtained using the predetermined screening criteria suggested in the Suzaku ABC guide.[7] The data reduction was carried out following the suggested techniques in the same ABC guide. We applied the barycentric correction to all event files using `aepipeline`. For the HXD/PIN data, simulated "tuned" non-X-ray-background

[7] http://heasarc.gsfc.nasa.gov/docs/suzaku/analysis/abc/

Table 1
Suzaku Observations of the 23 XRB Pulsars Considered in This Study

Pulsar	No. of ObsIDs	Selected ObsID	Date	Duration (s)
Her X-1[a,c]	10	100035010	2005-10-05	36123
Cen X-3[a,b,c,d]	1	403046010	2008-12-08	97587
4U 1626-67	2	400015010	2006-03-09	102639
4U 0115+63	2	406049010	2011-07-08	42274
4U 1907+09	2	401057010	2006-05-02	58440
4U 1538-52[a]	1	407068010	2012-08-10	45955
GX 301-2	2	403044010	2008-08-25	11427
IGR J16393-4643	1	404056010	2010-03-12	50540
Vela X-1[a]	1	403045010	2008-06-17	104709
XTE J1946+274	1	405041010	2010-10-11	50731
1A 0535+262	3	404054010	2009-08-24	52000
1A 1118-616	2	403049010	2009-01-15	49667
4U 0114+65	1	406017010	2011-07-21	106492
GX 304-1	2	905002010	2010-08-13	5104
OAO 1657-415[a,d]	1	406011010	2011-09-02	84729
GRO J1008-57	3	902003010	2007-11-30	47746
4U 1909+07	1	405073010	2010-11-02	29298
4U 2206+54	1	402069010	2007-05-16	103976
KS 1947+300	2	908001020	2013-11-22	7639
EXO 2030+375	2	402068010	2007-05-14	57607
SMC X-1[a,c]	10	706030080	2011-11-10	19859
Cep X-4	2	409037010	2014-06-18	29764
SW J2000.6+3210	1	4010530010	2006-04-12	12438

Notes.
[a] Eclipsing pulsars.
[b] Time filtered to exclude eclipses and dips.
[c] Orbital motion corrected.
[d] Period derivative included.

(NXB) event files, corresponding to the month and year of the respective observations, were used to estimate the NXB.[8]

In order to correct for Doppler shift of the pulse period due to the orbital motion of pulsars with smaller orbits, such as Her X-1, SMC X-1, and Cen X-3, and those with larger eccentricity such as OAO 1657-415, we corrected for arrival times in the PIN lightcurves of individual observations using orbital parameters taken from M. Falanga et al. (2015) and extrapolated to the time of each observation. We then plotted the pulse profile of each pulsar in small time segments in order to investigate whether the correction was successful. In cases where we found a drift in the pulse profile, this necessitated the introduction of a period derivative term to correct for residual Doppler shifts.

The sources considered in the present study and the ObsIDs corresponding to the observations used are listed in Table 1; we also note how many ObsIDs each pulsar has in the Suzaku archive (of which we typically used the one with the longest duration) and the type of timing correction if applicable. The X-ray binary types, the spin periods, and the inclination angles reported in the literature are listed in Table 2.

3. Modeling the X-Ray Pulse Profiles

The code Polestar (R. Cappallo et al. 2017) was designed to fit empirically a realization of the fan and pencil beam emission paradigm and to promptly parameterize large libraries of X-ray pulse profiles. The fitted parameters can then be analyzed statistically, as for example in R. C. Cappallo et al. (2020), who obtained a consistent solution for SXP 1062 by overcoming model degeneracies and profile changes to home in on the underlying geometry of the system.

In its default configuration, Polestar arranges the magnetic poles (hot spots) in a dipole whose magnetic axis is tilted relative to the NS rotation axis although it also passes through the NS center. This antipodal geometry can be selectively loosened to the extent of being able to position the hot spots at arbitrary locations on the NS surface. Each hot spot possesses both a fan-beam and a pencil-beam component, and radiation emission is axisymmetric with respect to the normal vector on the NS surface at each hot spot. In nonantipodal geometries, this choice is modified to make the beams axisymmetric with respect to the chord joining the two misaligned hot spots, i.e., following the magnetic field lines near the magnetic axis of the offset dipole. The default antipodal configuration was used in the experiments presented here.

Our modeling approach followed the methodology of R. Cappallo et al. (2017) and R. C. Cappallo et al. (2020); it is briefly summarized here. Each observed pulse profile was fitted without any priors being applied to the free model parameters. This model has six free parameters: (1) the inclination angle i, which is allowed to vary between 0° and 90°; (2) the latitude of the primary hot spot γ (0°–90°); (3) the longitude of the primary hot spot θ (0°–360°); (4) the power of the cosine (pencil) emission function (1–9); (5) the power of the sine (fan) emission function (1–9); and (6) the ratio of pencil to fan contribution to the total emission.

Polestar also accounts for GR light-bending effects by using the approximation of A. M. Beloborodov (2002) with the NS

[8] http://heasarc.gsfc.nasa.gov/docs/suzaku/analysis/pinbgd.html

Table 2
XRB Pulsars in Our Double-blind Study, Their Orbital Inclinations as Reported in the Literature, and Their NS Spin-axis Inclinations as Determined from the Polestar Model Fits

Source Name	XRB Type	Eclipsing System?	Spin Period P_{spin} (s)	Inclination in Literature i_{orbit} (deg)	Polestar Model Fits i_{spin} (deg)
Her X-1	IMXB	Y	1.24	80.5 ± 3.8[a]	55.0 ± 1.1
Cen X-3	SG	Y	4.82	70.2 ± 2.7[b]	74.0 ± 1.2
4U 1626-67	LMXB	...	7.66	11–36[c]	9.6 ± 2.2
4U 0115+63	Be	...	3.61	40–60[d]	52.9 ± 2.1
4U 1907+09	SG	...	483	55–70[e]	63.6 ± 3.0
4U 1538-52	SG	Y	530	72.6 ± 4.2[f]	76.5 ± 0.9
GX 301-2	SG	...	681	55–75[g]	78.6 ± 1.1
IGR J16393-4643	SG	...	910	39–77[h]	12.7 ± 1.9
Vela X-1	SG	Y	283	83.6 ± 3.1[i]	88.8 ± 3.0
XTE 1946+274	Be	...	15.83	>46[j]	80.1 ± 1.3
1A 0535+262	Be	...	104	35–39[k]	79.3 ± 1.1
1A 1118-61	Be	...	405	14.6 ± 1.2[l]	45.4 ± 2.1
4U 0114+65	SG	...	9391.19	45–50[m]	46.1 ± 1.3
GX 304-1	Be	...	272	60–80[n]	22.2 ± 1.7
OAO 1657-415	SG	Y	37.7	60–90[o]	25.9 ± 1.1
GRO J1008-57	Be	...	93.5	26–46[p]	47.1 ± 2.1
4U 1909+07	SG	...	438	38–72[q]	66.4 ± 1.1
4U 2206+54	SG	...	5554	<25[r]	21.7 ± 0.9
KS 1947+300	Be	...	2.763	28–57[s]	12.1 ± 0.8
EXO 2030+375	Be	...	41.7	48–57[t]	57.0 ± 1.0
SMC X-1	SG	Y	0.717	67.8 ± 4.2[u]	77.3 ± 1.4
Cep X-4	Be	...	66	unknown	12.3 ± 0.8
SW J2000.6+3210	Be	...	890	unknown	50.0 ± 4.2

Notes. The bottom two pulsars had no inclination reported in the literature.
[a] Model the eclipse duration to obtain eclipse half-angle and find orbital inclination for known masses of companion and NS (M. L. Rawls et al. 2011).
[b] Radial velocity curves since the system is eclipsing (T. D. C. Ash et al. 1999).
[c] From orbital solution of long X-ray observations (J. Middleditch et al. 1981; A. Levine et al. 1988).
[d] The mass and spectral type of the companion star were determined from optical observations and inclination derived for reasonable mass function (I. Negueruela & A. T. Okazaki 2001).
[e] Lack of an observed eclipse along with X-ray spectral analysis to find orbital variation of absorption due to the accretion stream (M. H. van Kerkwijk et al. 1989; M. S. E. Roberts et al. 2001).
[f] Model the eclipse duration to obtain eclipse half-angle and find orbital inclination for known masses of companion and NS (M. L. Rawls et al. 2011).
[g] Wind and stream model fits to the RXTE/ASM lightcurve along with variation in column density (D. A. Leahy & M. Kostka 2008);
[h] Get eclipse semiangle from orbital intensity profile from BAT lightcurves and assume companion mass (N. Islam et al. 2015; S. Kabiraj et al. 2020).
[i] Model the eclipse duration to obtain eclipse half-angle and find orbital inclination for known masses of companion and NS (M. L. Rawls et al. 2011; P. Kretschmar et al. 2021).
[j] Fits of the measured pulse frequencies and arrival times to derive orbital parameters and then estimated inclination for an assumed mass function (C. A. Wilson et al. 2003).
[k] Fitting optical line profiles (F. Giovannelli et al. 2007).
[l] Orbital elements determined from X-ray observations combined with an estimate of the mass of the optical companion (R. Staubert et al. 2011).
[m] Orbital solution plus known masses of companion and NS (E. D. Grundstrom et al. 2007).
[n] Fitting the line profiles of Hα and Hβ emission lines (C. Malacaria et al. 2017).
[o] Modeling the X-ray eclipse and from variation of absorption column density (M. Denis et al. 2005).
[p] Orbital solution from pulse periods, and disk parameters obtained from Hα emission line (M. J. Coe et al. 2007).
[q] Doppler delay (A. M. Levine et al. 2004).
[r] N. Masetti et al. (2004).
[s] Fits of the measured pulse frequencies and arrival times to derive orbital parameters and then estimated inclination for an assumed mass function (D. K. Galloway et al. 2004).
[t] Fits of the measured pulse frequencies and arrival times to derive orbital parameters and then estimated inclination for an assumed mass function (C. A. Wilson et al. 2008; E. Laplace et al. 2017).
[u] Model the eclipse duration to obtain eclipse half-angle and find orbital inclination for known masses of companion and NS (M. L. Rawls et al. 2011).

mass and radius set to their canonical values (1.4 $M_\odot$ and 10 km, respectively). The model is fitted to pulse profile data sets using the modified coordinate descent algorithm described in P. Bianchi et al. (2014).

The results of the fitting procedure for the 21 Suzaku pulse profiles with previously reported orbital inclination angles are shown in Figure 2. In each case, the contribution of each individual hot spot is also shown. Our best-fit spin-axis inclination angles are included in Table 2. Parameter uncertainties were obtained by bootstrap resampling: At each iteration, we replace the flux values $f(i)$ in the binned profile with a new value $f'(i)$ drawn from a normal distribution with mean $f(i)$ and standard deviation $\sigma(i)$. The Polestar fit is repeated on this resampled profile, and the best-fit parameters are recorded. After 1000 iterations, we generate the probability distribution of each free parameter, and we measure the mean,

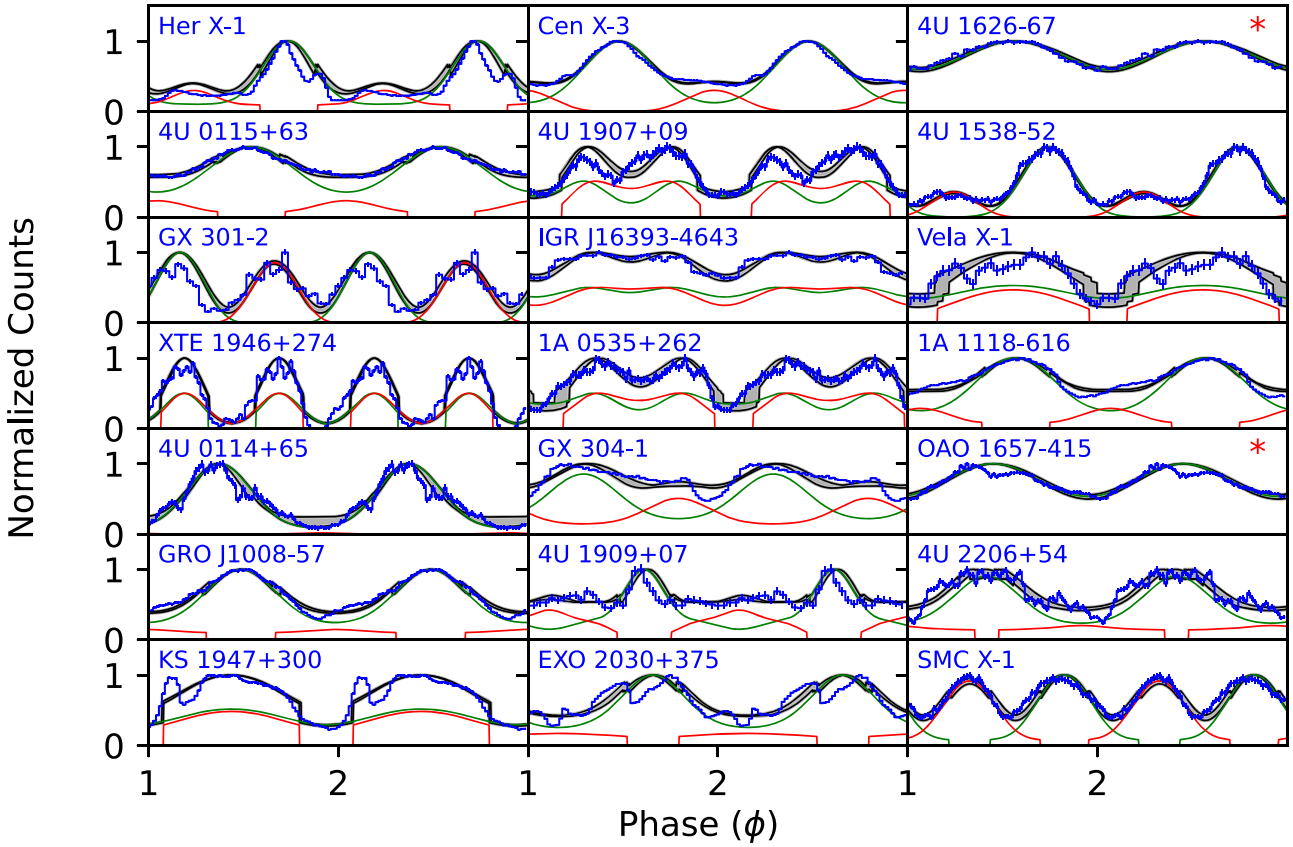

Figure 2. Polestar model fits to the 21 Suzaku pulse profiles with previously reported orbital inclination angles. The phase-binned X-ray data are plotted in blue with error bars; the model best fits are between the black lines, whereas the contributions from the primary and secondary hot spots are shown by green and red lines, respectively (the two profiles marked by a red asterisk in the upper right-hand corner have only one hot spot visible at any time). Uncertainties in the models are depicted by gray envelopes representing standard deviations obtained from 1000 bootstrap iterations in each case.
(The data used to create this figure are available in the online article.)

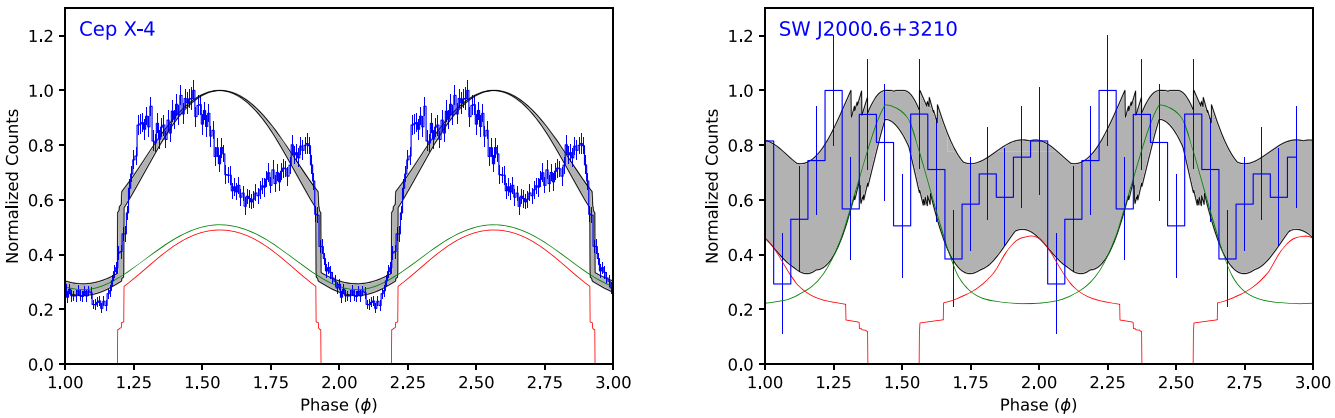

Figure 3. As in Figure 2, for the two Suzaku pulse profiles in our sample that do not have reported inclination angles.
(The data used to create this figure are available in the online article.)

standard deviation, and 95% confidence interval. In our models, the resulting uncertainties in i were typically found to be of the order of a few degrees.

Two additional pulse profiles (Cep X-4 and SW J2000.6 +3210, listed at the bottom of Table 1) were eliminated from the statistical analysis because orbital inclination angles could not be found in the literature. These profiles were, however, fitted with Polestar since they were included in the blind study. Model fits are shown in Figure 3, and their best-fit inclination angles are reported in Table 2.

4. Statistical Analysis

4.1. Probabilities for Chance Compliance

Comparing the Polestar inclination fits to the binary orbital inclination values reported in the literature, we find broad

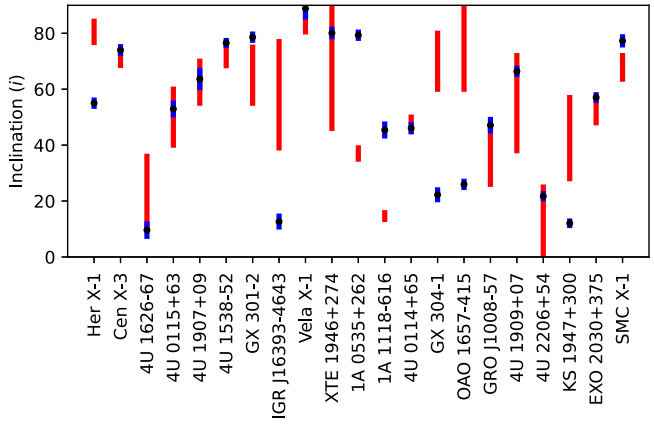

Figure 4. Spin-axis inclination angles obtained by Polestar blind-fitting to Suzaku pulse profiles for 21 XRB pulsars. The red lines denote the range of orbital-plane inclination angles ($i_{\rm orbit}$) reported in the literature, and the black dots are the spin-axis angles obtained by Polestar ($i_{\rm spin}$), with their 1σ uncertainties represented in blue. These two determinations disagree clearly in only 7 of the 21 systems (differences larger than 15°).

agreement in 14 of the 21 cases, as can be seen by inspecting Figure 4. The corresponding ranges overlap in 12 systems, and the minor gaps in the remaining two systems are narrower than 4°. In contrast, the large gaps in the remaining seven systems, in which we see clear disagreement, extend from 15° to 40° in a nearly uniform distribution.

We have applied two independent statistical tests to evaluate the probability of Polestar getting m out of n compliant inclinations by chance, considering that each of the n cases has a different probability of success p_k ($k = 1, 2, \cdots, n$). The probability p_k of guessing any particular inclination value θ_k by chance is $\Delta\theta_k/90°$, where $\Delta\theta_k$ is the uncertainty range corresponding to θ_k. We have performed an analytic calculation following the methodology of the Poisson-binomial distribution (e.g., Y. H. Wang 1993; M. Fernandez & S. Williams 2010; Y. Hong 2013; details below) and also a set of Monte Carlo simulations: at each iteration, a set of $n = 21$ random deviates are drawn from the interval 0°–90°, and they are compared against the literature set of known (θ_k, $\Delta\theta_k$) pairs to determine the number m of successful draws. After 10^7 repetitions, we plot the frequency histogram of m to determine the fraction of trials producing $m = 0, 1, 2, \cdots$ successful outcomes, as shown in Figure 5.

External validation of the pulse-profile fitting process relies on comparing the Polestar inclination angles against independent values obtained from the literature. Since the literature values for each XRB have varying uncertainties, the commonly used binomial distribution of m successes in n trials is not applicable. For the probability mass function (PMF) of our experiments, we used a recent stable algorithm (M. Fernandez & S. Williams 2010; Y. Hong 2013) for the Poisson-binomial distribution (Y. H. Wang 1993), viz.,

$$Pr(m;\, n) = \frac{1}{n+1}\sum_{\ell=0}^{n} C^{-\ell m} \prod_{k=1}^{n} [1 + (C^{\ell} - 1)\, p_k], \qquad (1)$$

where

$$C = \exp\left(\frac{2\pi i}{n+1}\right). \qquad (2)$$

Here $i = \sqrt{-1}$; the indices k, $m = 1, 2, 3, \cdots, n$; index $\ell = 0, 1, 2, \cdots, n$; and $p_k \equiv \Delta\theta_k/90°$ represents the individual probabilities of success in n independent yes/no experiments. The uncertainty ranges $\Delta\theta_k$ of inclinations θ_k were obtained from the $i_{\rm orbit}$ column in Table 2. The $m = 0$ probability of complete failure was calculated from the simpler formula

$$Pr(0;\, n) = \prod_{k=1}^{n} (1 - p_k). \qquad (3)$$

The well-known binomial distribution emerges when all p_k values are equal. The values resulting from Equation (1) must be real; any deviation of the imaginary part from zero indicates the magnitude of the approximation error, which in our calculations turned out to be negligible. The largest such error was $\varepsilon_{\rm max} = 3 \times 10^{-16}$ for $m = n = 21$.

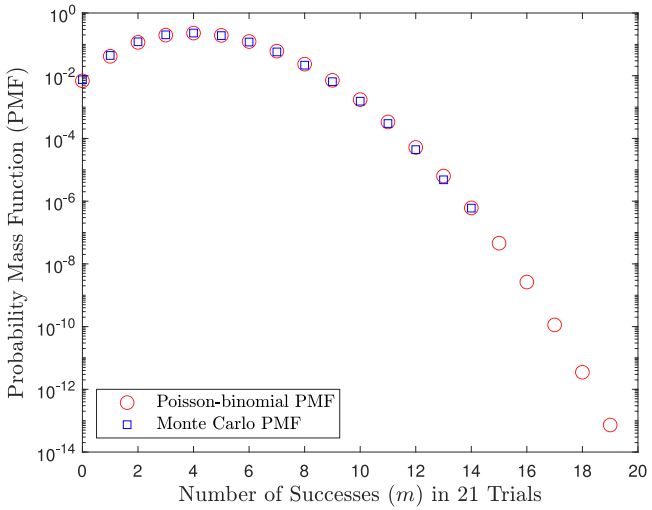

Figure 5. PMF for obtaining m compliant inclination angles by chance when considering the 21 reported values and their uncertainty ranges obtained from the literature. According to this analysis, the probability that Polestar could have been successful by chance in 14+ of 21 cases is only 6.6×10^{-7}. Thus, the alignment of NS spin and orbital angular momentum vectors seen in 14 of the 21 binary systems in Figure 4 is also supported by formal statistical analyses (the Poisson-binomial distribution and Monte Carlo experiments).

For illustration purposes, we have calculated the PMF $Pr(m; 21)$ for $m = 0, 1, 2, \cdots, 19$. For the next two higher values ($m = 20, 21$), the chance probabilities are negligible ($\sim\varepsilon_{\rm max}$), whereas the last calculated value is $Pr(19; 21) = 7.3 \times 10^{-14}$ ($\sim 250\varepsilon_{\rm max}$). The results are shown in Figure 5 along with the empirical probabilities obtained from the Monte Carlo simulations. The PMF peaks at $m = 4$, where $Pr(4; 21) = 0.23$. The probabilities of Polestar matching 14 or 14+ inclinations by chance (with an antipodal geometry of the magnetic poles) are 6.1×10^{-7} and 6.6×10^{-7}, respectively. For comparison, in the strict compliant case of 12 or 12+ overlapping ranges by chance, the probabilities increase by factors of 85 and 89, respectively; yet, they remain negligibly small, pointing again to the physical nature of the Polestar results.

4.2. A Stringent Test for Compliance

In a more stringent test of compliant inclinations, we find that the mean Polestar values land within the ranges of orbital inclinations quoted in the literature in precisely 8 of the 21 cases (Figure 4 and Table 2). The PMF shown in Figure 5 indicates that the corresponding chance probability for 8+ such highly successful overlaps is about 0.033. At the standard $\alpha = 0.05$ significance level, this p-value suggests that we should accept the

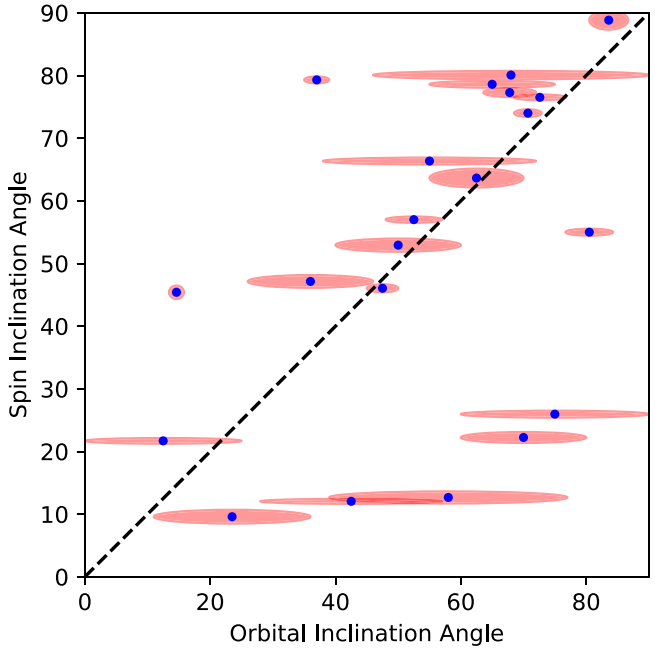

Figure 6. Spin inclination angle ($i_{\rm spin}$) vs. orbital inclination angle ($i_{\rm orbit}$) for the 21 XRBs in this study. The semimajor and semiminor axes of the ellipses correspond to the uncertainties in $i_{\rm orbit}$ and $i_{\rm spin}$, respectively. The dashed line represents $R = 1$ in Equation (4), the expected value for the XRB population under the null hypothesis.

alternative hypothesis that the observed spin–orbit alignment is not due to chance in our sample of 21 XRB sources—but see also Section 4.4, where a battery of χ^2 tests show undoubtedly that not all XRBs obey spin–orbit alignment.

4.3. Eclipsing Binaries

In our analysis, we have also considered separately the six known eclipsing binary systems in our sample, which have orbital inclinations higher than about 68°; these are marked by *a* in Table 1 and by Y in Table 2. Polestar determined compliant inclinations in $m = 4$ of these six highly inclined (mostly SG) XRBs. The PMF peaks at $m = 0$, where $Pr(0; 6) = 0.44$, followed by $Pr(1; 6) = 0.41$. Thus, the most probable outcomes by chance would be no match for any of these six systems, or one match at best.

The chance probabilities for four or more than four matches in six trials are 1.54×10^{-3} and 1.60×10^{-3}, respectively. In the strict compliant case of three or more than three matches by chance, the probabilities finally rise to more meaningful values of about $p = 0.02$. The approximation errors indicated by the imaginary parts of the PMF values are smaller in this case compared to the $n = 21$ case above (considerably fewer terms are involved in Equation (1) for $n = 6$); the largest error here is $\varepsilon_{\rm max} = 1.43 \times 10^{-16}$ for $m = 3$. In this case as well, the *p*-values show that matching by chance three or four inclinations in six eclipsing binaries is highly improbable.

4.4. Reduced χ^2 Tests of Inclination Ratios

As a complementary statistical test, we have carried out hypothesis testing of the inclination ratios

$$R \equiv \frac{i_{\rm spin}}{i_{\rm orbit}}, \tag{4}$$

using the χ^2 statistic (J. R. Taylor 1997; R. Andrae et al. 2010). The expected value for compliant inclinations is $R = 1$. This is depicted by a dashed line in Figure 6 that shows the data points and their uncertainties in inclination space. The variances of the R ratios for the 21 data points were calculated from Equation (4) by using error propagation and the 1σ uncertainties listed in Table 2.

The data in Table 2 and Figure 6 indicate no overlap ($R \neq 1$) for nine inclination pairs for which the range of their R ratios is given by

$$R \in [0.374, 0.731] \bigcup [1.054, 2.741],$$

as determined from the smallest inclination °.differences Δi (the vertical gaps seen between inclination error bars in Figure 4), viz.,

$$\Delta i \equiv (i_{\rm spin} - i_{\rm orbit}) \in [-36.^\circ 1, -15.^\circ 1] \bigcup [2.^\circ 5, 39.^\circ 2].$$

These Δi ranges are discussed in Section 5.2 below.

For the R ratios, our two adopted assumptions are designed to consistently favor the null hypothesis H_0 ($R = 1$): we allow $R \neq 1$ only for the nine deviant points, and we minimize the differences of these $R \neq 1$ ratios from $R = 1$ by using the known inclination error bars. Under these assumptions (that are heavily biased in favor of H_0), the statistical outcomes are as follows:

(a) *Total sample*. In our sample of $n = 21$ sources, the number of degrees of freedom is $d = n - 1 = 20$, and the reduced test statistic is found to be

$$\chi^2 = \frac{1}{d}\sum_{k=1}^{n}\frac{(R_k - 1)^2}{\sigma_k^2} = \frac{337.4}{20} = 16.87, \tag{5}$$

where σ_k^2 is the variance corresponding to the ratio R_k ($k = 1, 2, \cdots, n$). For the confidence level of $\alpha = 0.001$ (or 99.9%), the reduced critical value is $\chi^2_{\rm crit} = 2.266$ for a two-tailed test. Since $\chi^2 \gg \chi^2_{\rm crit}$, we reject H_0 at the 99.9% confidence level—that is, the null hypothesis that the entire population of XRBs is characterized by $R = 1$. This could be a strong indication that not all XRBs have their spin and orbital axes aligned (see also Section 5.5).

The large value of the reduced χ^2 implies that H_0 should be rejected outright despite the fact that the test was biased in favor of H_0. For this reason, the same conclusion holds strong for a fair test, in which we use all 21 data points, and we calculate R ratios from the midpoints of the inclination ranges listed in Table 2. In this case, we find that $\chi^2 = 655/20 = 32.75$, leading to the rejection of H_0 as well.

(b) *Eclipsing binaries*. In the much smaller sample of $n = 6$ eclipsing binaries (three of which have overlapping inclinations), then, $d = 5$, and the reduced test statistic $\chi^2 = 87.67/5 = 17.53$ is found to be much higher than the reduced critical value of $\chi^2_{\rm crit} = 4.102$ at the $\alpha = 0.001$ level. Thus, at the 99.9% confidence level, we reject H_0—that is, the null hypothesis that $R = 1$ in all eclipsing XRBs as well. This conclusion also holds for the corresponding fair test, in which we use all six data points, and we calculate R ratios from the midpoints of the inclination ranges listed in Table 2. In this case, we find that $\chi^2 = 175/5 = 35$ leads again to the rejection of H_0 in eclipsing binaries.

(c) *Degeneracies*. Qualitatively, Figure 6 shows that approximately two-thirds of the sample cluster along the

diagonal line denotes aligned rotation. The correlation is notably stronger for spin inclination angles >45°. We can think of no physical reason why this should be so; therefore, some bias or systematic error in the modeling methodology could be suspected. The pioneering work of A. M. Beloborodov (2002) discusses a degeneracy in the (inclination, magnetic obliquity) parameter space, and it could be that such a systematic error is at work here, especially since we fitted only one pulse profile from each system. Modeling of an expanded sample of pulse profiles for each pulsar can be used to explore this issue and possibly resolve the inclination ambiguity (R. Cappallo et al. 2017).

5. Discussion

5.1. Pulse Profiles

X-ray pulse profiles hold some important clues about the associated accretion flows and the underlying X-ray beaming geometry. While some pulsars show stable pulse profiles on timescales of years, in systems which experience large variations in accretion rate, their pulse profiles change markedly with luminosity (A. N. Parmar et al. 1989). At high accretion rates, pulse profiles can show strong energy dependence, with some pulsars even exhibiting phase reversals of up to 180° in going from lower to higher photon energies (A. Beri et al. 2014). Energy dependence in some cases can be isolated to specific spectral features including iron lines and cyclotron resonant scattering (see, e.g., S. S. Tsygankov et al. 2006; R. Staubert et al. 2019; C. Ferrigno et al. 2023) and at soft energies by thermal emission (e.g., N. La Palombara et al. 2018a, 2018b) although the latter soft effects would not materialize in the Suzaku HXD band.

Dips at some phases could indicate obfuscation by the inflowing accretion stream (C. Maitra & B. Paul 2013). Furthermore, the long-term stability of the pulse profiles can also provide important clues about the emission processes near the surface of the pulsar. The Fourier decomposition technique can be used to investigate the stability of the X-ray pulse profile by studying the relative amplitudes and the phase differences of its harmonic components with respect to the fundamental (see, e.g., P. Pradhan et al. 2015; J. Alonso-Hernández et al. 2022).

The profiles presented in Figure 2 show a variety of morphologies ranging from the simple sinusoid (e.g., 4U 1626-67, 4U 0115+63) to double-peaked with both peaks of roughly equal height and equal separation (e.g., Vela X-1, SMC X-1) or a sharp primary peak with a weaker secondary peak (e.g., Her X-1, 4U 1538-52) to double-peaked with the peaks fused into a very broad feature (e.g., 4U 1907+09, XTE 1946+274). Polestar model fits are able to reproduce these gross features reasonably well, despite the inherent lack of detailed physics and the imposed restriction of antipodal magnetic field geometry. As has been previously noted by others (e.g., U. Kraus et al. 1996), profiles that do not possess a symmetry point cannot be reproduced by such centered dipoles and require the dipoles to be offset from the NS centers or the hot spots to be asymmetrically displaced. As an example of such an asymmetry, the double peaks of GX 301-2 are not equally spaced in phase.

Two pulsars (4U 1626-67 and OAO 1657-415) are fit by models that require only a single hot spot to be visible (marked by asterisks in Figure 2). The inclination angles are small ($10° \pm 2$, and $26° \pm 1$) such that the other pole is perpetually hidden. For 4U 1626-67, this is consistent with the published orbital inclination angle (11°–36°). On the other hand, OAO 1657-415 is an eclipsing system, which consequently requires a large misalignment. However, its pulse profile contains a dip where the model predicts peak flux, so some caution should be exercised in future investigations.

5.2. Inclination Angles

Comparing the inclination angles produced by Polestar to those found in the literature, 14 out of 21 are in broad agreement (Figure 4). Two independent statistical methods (Poisson-binomial and Monte Carlo) produced nearly identical distributions (Figure 5), in which the probability of 14 Polestar successes being due to chance is 6.1×10^{-7} and the probability to get 14+ successes is 6.6×10^{-7}. Model uncertainties obtained by bootstrap resampling are of order of a few degrees, so they are not large enough to materially affect the number of compliant matches. These matches include two XRB systems (GX 301-2 and SMC X-1) with inclinations very close (to within <4°) to those quoted in the literature, while the seven failures to match show absolute discrepancies of about 15°–40° (Table 2 and Section 4.4). Furthermore, Vela X-1 is an established, very highly inclined system, a result also borne out by this work.

That the pulsar spin axes are predominantly perpendicular to their orbital planes is by no means an obvious assertion although such an alignment is routinely assumed in HMXB investigations. During the SN that creates the NS, asymmetries in the detonation are widely thought to impart a kick velocity to the relic. Numerous lines of observational evidence for SN kicks exist, including the facts that HMXBs tend to have elliptical orbits, that the separation of the relic from the SN remnant grows with age, and that the bimodal spin–orbit distributions point to two different SN channels (C. Knigge et al. 2011) that were recently linked to systematically differing space velocities in the Gaia data (M. Prišegen 2020).

5.3. Tidal Forces and Torques

Compared to the strong forces required to accelerate, distort, or even break up a close binary system, reorienting the NS spin axis requires only a modest impulse. A remarkable, yet overlooked, observation is that, in several Be-HMXBs, the equatorial disk of the Be star appears to lie far out of the orbital plane (e.g., SXP214; J. Hong et al. 2016), even to the extent of being nearly orthogonal to it (e.g., SXP 1062; A. González-Galán et al. 2018). If a massive B star can be knocked off on its side, the much smaller moment of inertia of an NS would seem to raise the likelihood of substantially misaligned pulsar spins in HMXBs. Accretion torques can act in either sense, to "right" the pulsar or tip it entirely out of alignment (Y. M. Wang 1981) on long timescales that increase with orbital separation (as also do the tidal circularization timescales of the orbits).

5.4. Toward Tighter Mass Functions

The results described in Section 4 suggest that in many cases,

$$i_{\rm spin} \simeq i_{\rm orbit} \tag{6}$$

so that PPM-derived inclinations could be used in some cases to resolve the $\sin(i)$ ambiguity in the mass function derived from Kepler's third law. Knowledge of inclination can tighten

dramatically the mass functions determined by other methods (optical Doppler spectroscopy, pulse timing, and photometry), as in many cases, the orbital inclinations are subject to large uncertainties (as seen in the red error bars of Figure 4). Our results show that even a single pulse-profile fit at high S/N ratio can provide a quite accurate $i_{\rm spin}$ value. Naturally, more work is needed to examine whether this technique would work better for certain subsets of the Galactic XRB pulsar sample.

5.5. Comparisons

Contrasting our results with those of R. C. Cappallo et al. (2020), who used dozens of profiles to obtain a consistent set of physical parameters for a single pulsar (SXP 1062, a Be-XRB pulsar in the SMC), the Galactic sources have a uniformly higher S/N ratio, and they include many SG systems whose more consistent behavior may turn out to be an advantage in Polestar modeling.

As a cautionary note, we recognize that if two-thirds of the spin-derived inclinations do match up with the known orbital inclinations and one-third do not (Figure 4), then one must be careful in adopting our result blindly for any given individual system. In fact, we do not expect that relation (6) has been established in all XRBs because of the many processes working for and against such an alignment (A. Biryukov & P. Abolmasov 2021). This expectation is supported by the outcome of the reduced χ^2 test for our sample of 21 XRBs (Section 4.4); the rejection of the null hypothesis (Equation (6)) at the 99.9% confidence level stipulates that, in practice, we should not expect spin–orbit alignment to hold for the entire population of XRBs. Thus, the 2/3 ratio of aligned inclinations in (mostly) HMXBs emerges as the principal result of our study (see also Section 4).

The occurrence of epoch/luminosity variability in the pulse profiles shapes of X-ray pulsars is widely known and has been reported concretely for some of the targets of this paper. The change of the pulse profile shapes could affect significantly the estimation of the orbital inclination angle as well as the angle between the spin axis and the magnetic dipole axis. As shown in R. Cappallo et al. (2019), such variability can produce a spread of the orbital inclination values for each source. This can be viewed as a systematic error or as real changes in the apparent angle between the spin axis and dipole axis produced by physical processes, such as movement of the hot spot within the polar-cap accretion column or changes in the shape and location of the column itself (G. S. Miller 1996; M. Sasaki et al. 2012).

6. Conclusions

We performed PPM on hard X-ray profiles obtained by Suzaku/HXD for 23 XRB pulsars. We used the Polestar modeling code, which implements a version of the well-known fan-beam and pencil-beam paradigm with approximate GR light bending also included. Although our implementation lacks detailed physics, it provides a useful framework to parameterize pulse-profile morphology and link it to structures in the NS magnetosphere. The model fits were conducted as part of a double-blind study, where no prior information was introduced to the code (initial conditions or specific ranges for the free parameters). The resulting synthetic profiles reproduced the overall shape of the Suzaku pulse profiles and yielded a set of best-fit parameter values for each XRB pulsar, including the inclination of the NS spin axis to our line of sight ($i_{\rm spin}$). We compared these inclination angles to the orbital inclination angles ($i_{\rm orbit}$) obtained from a literature search, resulting in 14 out of 21 cases of broad agreement (the remaining 2 of the 23 pulsars did not have inclinations in the literature). The ranges of reported values for $i_{\rm orbit}$ varied widely among the sample, so testing the probability that the observed level of agreement could have occurred by chance was carried out by means of Monte Carlo simulations, whose results were also supported by an analytic calculation based on the relevant Poisson-binomial distribution. Our main conclusion is that the spin and orbital angular momentum vectors are aligned in two-thirds of the XRB systems in our sample, while a clear discrepancy (15°–40°) was found in seven cases (Figure 4 and Table 2). Whether these cases are due to actual misalignment or additional properties of the pulse profiles not captured by the Polestar model is unclear. In fact, several of these pulsars have previously shown pulse-profile variations with luminosity and photon energy that were not accessible to this study that used a single observation of each pulsar in a single energy band. Such effects likely contribute to the scatter in the favored $i_{\rm spin}$–$i_{\rm orbit}$ relation (Equation (6)), and they provide a clear path for further studies of individual XRB sources.

Acknowledgments

We thank our anonymous referees for pointed comments and suggestions that helped us improve this paper and also work out the tests described in Section 4.4. This work was facilitated by NASA Astrophysics Data Analysis Program (ADAP) grants NNX14-AF77G and 80NSSC18-K0430 and by NSF-AAG grant 2109004.

Facility: Suzaku (ASTRO-EII).

Software: Polestar, Python, R, Matlab, SpaceEngine.

ORCID iDs

Silas G. T. Laycock https://orcid.org/0000-0002-8427-0766
Rigel C. Cappallo https://orcid.org/0000-0003-0267-8432
Pragati Pradhan https://orcid.org/0000-0002-1131-3059
Dimitris M. Christodoulou https://orcid.org/0000-0002-7652-2206
Biswajit Paul https://orcid.org/0000-0002-8775-5945

References

Alonso-Hernández, J., Fürst, F., Kretschmar, P., Caballero, I., & Joyce, A. M. 2022, A&A, 662, A62
Andrae, R., Schulze-Hartung, T., & Melchior, P. 2010, arXiv:1012.3754
Ash, T. D. C., Reynolds, A. P., Roche, P., et al. 1999, MNRAS, 307, 357
Basko, M. M., & Sunyaev, R. A. 1976, MNRAS, 175, 395
Becker, P. A., & Wolff, M. T. 2005, ApJ, 630, 465
Becker, P. A., & Wolff, M. T. 2007, ApJ, 654, 435
Beloborodov, A. M. 2002, ApJL, 566, L85
Beri, A., Jain, C., Paul, B., & Raichur, H. 2014, MNRAS, 439, 1940
Beskin, V. S. 2018, PhyU, 61, 353
Beskin, V. S., Chernov, S. V., Gwinn, C. R., & Tchekhovskoy, A. A. 2015, SSRv, 191, 207
Bianchi, P., Hachem, W., & Iutzeler, F. 2014, arXiv:1407.0898
Biryukov, A., & Abolmasov, P. 2021, MNRAS, 505, 1775
Blum, S., & Kraus, U. 2000, ApJ, 529, 968
Cappallo, R., Laycock, S. G. T., & Christodoulou, D. M. 2017, PASP, 129, 124201
Cappallo, R., Laycock, S. G. T., Christodoulou, D. M., Coe, M. J., & Zezas, A. 2019, MNRAS, 486, 3248
Cappallo, R. C., Laycock, S. G. T., Christodoulou, D. M., et al. 2020, MNRAS, 495, 2152

Christodoulou, D. M., Laycock, S. G. T., & Kazanas, D. 2017, MNRAS, 470, L21
Christodoulou, D. M., Laycock, S. G. T., Yang, J., & Fingerman, S. 2016, ApJ, 829, 30
Coe, M. J., Bird, A. J., Hill, A. B., et al. 2007, MNRAS, 378, 1427
Coley, J. B., Corbet, R. H. D., & Krimm, H. A. 2015, ApJ, 808, 140
Corbet, R. H. D. 1984, A&A, 141, 91
Denis, M., Bulik, T., & Marcinkowski, R. 2010, AcA, 60, 75
Doroshenko, V., Poutanen, J., Tsygankov, S. S., et al. 2022, NatAs, 6, 1433
Falanga, M., Bozzo, E., Lutovinov, A., et al. 2015, A&A, 577, A130
Falkner, S. 2018, PhD thesis, Friedrich Alexander Univ. Erlangen-Nuremberg, Germany
Fernandez, M., & Williams, S. 2010, ITAES, 46, 803
Ferrigno, C., D'Ai, A., & Ambrosi, E. 2023, A&A, 677, A103
Galloway, D. K., Morgan, E. H., & Levine, A. M. 2004, ApJ, 613, 1164
Giovannelli, F., Bernabei, S., Rossi, C., & Sabau-Graziati, L. 2007, A&A, 475, 651
González-Galán, A., Oskinova, L. M., Popov, S. B., et al. 2018, MNRAS, 475, 2809
Grundstrom, E. D., Blair, J. L., Gies, D. R., et al. 2007, ApJ, 656, 431
Hong, J., Antoniou, V., Zezas, A., et al. 2016, ApJ, 826, 4
Hong, Y. 2013, Computational Statistics and Data Analysis, 59, 41
Hu, Y. F., Ji, L., Yu, C., et al. 2023, ApJ, 945, 138
Ikhsanov, N. R. 2007, MNRAS, 375, 698
Islam, N., Maitra, C., Pradhan, P., & Paul, B. 2015, MNRAS, 446, 4148
Kabiraj, S., Islam, N., & Paul, B. 2020, MNRAS, 491, 1491
Kalapotharakos, C., Wadiasingh, Z., Harding, A. K., & Kazanas, D. 2021, ApJ, 907, 63
Kalapotharakos, C., Wadiasingh, Z., Harding, A. K., & Kazanas, D. 2022, ApJ, 934, 65
Klus, H., Ho, W. C. G., Coe, M. J., Corbet, R. H. D., & Townsend, L. J. 2014, MNRAS, 437, 3863
Knigge, C., Coe, M. J., & Podsiadlowski, P. 2011, Natur, 479, 372
Kokubun, M., Makishima, K., Takahashi, T., et al. 2007, PASJ, 59, 53
Koyama, K., Tsunemi, H., Dotani, T., et al. 2007, PASJ, 59, 23
Kraus, U., Blum, S., Schulte, J., Ruder, H., & Meszaros, P. 1996, ApJ, 467, 794
Kraus, U., Nollert, H.-P., Ruder, H., & Riffert, H. 1995, ApJ, 450, 773
Kraus, U., Zahn, C., Weth, C., & Ruder, H. 2003, ApJ, 590, 424
Kretschmar, P., El Mellah, I., Martínez-Núñez, S., et al. 2021, A&A, 652, A95
Kunieda, H., Mitsuda, K., Takahashi, T., Kelley, R., & White, N. 2006, Proc. SPIE, 6266, 626605
La Palombara, N., Esposito, P., Mereghetti, S., et al. 2018a, MNRAS, 475, 1382
La Palombara, N., Esposito, P., Pintore, F., et al. 2018b, A&A, 619, A126
Laplace, E., Mihara, T., Moritani, Y., et al. 2017, A&A, 597, A124
Leahy, D. A., & Kostka, M. 2008, MNRAS, 384, 747
Levine, A., Ma, C. P., McClintock, J., et al. 1988, ApJ, 327, 732
Levine, A. M., Rappaport, S., Remillard, R., & Savcheva, A. 2004, ApJ, 617, 1284
Maitra, C., & Paul, B. 2013, ApJ, 763, 79
Malacaria, C., Kollatschny, W., Whelan, E., et al. 2017, A&A, 603, A24
Masetti, N., Dal Fiume, D., Amati, L., et al. 2004, A&A, 423, 311
McBride, V. A., Coe, M. J., Negueruela, I., Schurch, M. P. E., & McGowan, K. E. 2008, MNRAS, 388, 1198
Middleditch, J., Mason, K. O., Nelson, J. E., & White, N. E. 1981, ApJ, 244, 1001
Miller, G. S. 1996, ApJL, 468, L29
Miller, M. C., Lamb, F. K., Dittmann, A. J., et al. 2019, ApJL, 887, L24
Negueruela, I., & Okazaki, A. T. 2001, A&A, 369, 108
Okazaki, A. T., & Negueruela, I. 2001, A&A, 377, 161
Parmar, A. N., White, N. E., & Stella, L. 1989, ApJ, 338, 373
Pétri, J., Guillot, S., Guillemot, L., et al. 2023, A&A, 680, A93
Pétri, J., & Mitra, D. 2021, A&A, 654, A106
Pierbattista, M., Harding, A. K., Gonthier, P. L., & Grenier, I. A. 2016, A&A, 588, A137
Poutanen, J., Ibragimov, A., & Annala, M. 2009, ApJL, 706, L129
Pradhan, P., Paul, B., Paul, B. C., Bozzo, E., & Belloni, T. M. 2015, MNRAS, 454, 4467
Prišegen, M. 2020, A&A, 640, A86
Rawls, M. L., Orosz, J. A., McClintock, J. E., et al. 2011, ApJ, 730, 25
Reig, P. 2011, Ap&SS, 332, 1
Riley, T. E., Watts, A. L., Bogdanov, S., et al. 2019, ApJL, 887, L21
Roberts, M. S. E., Michelson, P. F., Leahy, D. A., et al. 2001, ApJ, 555, 967
Sasaki, M., Müller, D., Kraus, U., Ferrigno, C., & Santangelo, A. 2012, A&A, 540, A35
Staubert, R., Pottschmidt, K., Doroshenko, V., et al. 2011, A&A, 527, A7
Staubert, R., Trumper, J., Kendziorra, E., et al. 2019, A&A, 622, A61
Taylor, J. R. 1997, An Introduction to Error Analysis (2nd ed.; Sausalito, CA: Univ. Science Books)
Tsygankov, S. S., Lutovinov, A. A., Churazov, E. M., & Sunyaev, R. A. 2006, MNRAS, 371, 19
van Kerkwijk, M. H., van Oijen, J. G. J., & van den Heuvel, E. P. J. 1989, A&A, 209, 173
Wang, Y. H. 1993, Statistica Sinica, 3, 295
Wang, Y. M. 1981, SSRv, 30, 341
Wang, Y. M., & Welter, G. L. 1981, A&A, 102, 97
Watts, A. L., Andersson, N., Chakrabarty, D., et al. 2016, RvMP, 88, 021001
West, B. F., Wolfram, K. D., & Becker, P. A. 2017, ApJ, 835, 130
Wilson, C. A., Finger, M. H., & Camero-Arranz, A. 2008, ApJ, 678, 1263
Wilson, C. A., Finger, M. H., Coe, M. J., & Negueruela, I. 2003, ApJ, 584, 996